Effect of bainite layer by LSMCIT on wear resistance of medium-carbon bainite steel at different temperatures

X. L. Xing[a], X. M. Yuan[b], Y. F. Zhou[a, c]*, X. W. Qi[c], X. Lu[c], T. H. Xing[a], X. J. Ren[d], Q. X. Yang[a]*

[a] *State Key Laboratory of Metastable Materials Science & Technology, Yanshan University, Qinhuangdao 066004, P. R. China*

[b] *Hebei Provincial Key Laboratory of Heavy Machinery Fluid Power Transmission and Control, Yanshan University, Qinhuangdao 066004, P. R. China*

[c] *College of Mechanical Engineering, Yanshan University, Qinhuangdao 066004, P. R. China*

[d] *School of Engineering, Liverpool John Moores University, Liverpool L3 3AF, UK*

[*] Corresponding author, Tel: 86-335-8387471, Fax: 86-335-807-4545,

E-mail: yfzhou@ysu.edu.cn (Y. F. Zhou); qxyang@ysu.edu.cn (Q. X. Yang)

Abstract

In this work, bainite layer was prepared by Laser surface melting combined with isothermal treatment (LSMCIT) at 250ºC. The microstructures of the samples were analyzed by scanning electron microscopy (SEM), X-ray Diffraction (XRD) and transmission electron microscopy (TEM). Their wear resistances at 20ºC, 100ºC and 200ºC were measured using reciprocating tribometer. After the wear test, the confocal laser scanning microscope and SEM were used to characterize the topography of all abrasion surfaces, and the phase transformations occurred on the contact surfaces were analyzed by XRD. The results show that the microstructure of the LSMCIT sample has been refined to nanoscale. The wear volume reduction ratio of LSMCIT sample is 40.9% at 20ºC. The wear resistances of the samples are decreased with

increasing of the temperature, however, the decrease in amplitude of the bainite is relatively small. The harder surface of the LSMCIT sample can provides higher mechanical support, and the white-etching layer on surface are difficult to remove by the reciprocating friction. The wear resistances of the LSMCIT samples at 20ºC, 100ºC and 200ºC are excellent, which shows the wide temperature ranges in wear applications.

Keywords: Laser surface melting; bainite; retained austenite; wear resistance.

1. Introduction

Nanostructure carbide-free bainite are equipped with excellent strength and high hardness. Moreover, the nanobainite steels can be obtained by an uncomplicated manufacturing route [1, 2]. In nanobainite, the microstructure consist of exceptionally fine plates of bainitic ferrite (BF) and nanoscale carbon-enriched retained austenite (RA) film [3, 4]. The nanobainite can be obtained at low bainite transformation temperature when the carbon content of the steel is high. In this way, ultrahigh hardness levels of 600 HV and good combinations of strength and toughness can be obtained by transforming at temperatures as low as 200ºC [5]. The major goal of the nanobainite used in the industrial application is to obtain the high surface property parts that withstand large loads and without suffering damage [6]. Another important factor in the

widespread application of nanobainite is the excellent wear resistance.

It was reported that the abrasive wear exists greatly in mechanical equipments moving and machine assemblies, and approximately 50% of the material loss is due to abrasive wear [7]. The wear resistance of the bainite steel have been investigated largely. Bakshi et al. [8] found that the bainitic structure is hardened at the surface, and white-etching layer with martensitic transformation which causes wear resistance to increase. Chang [9] investigated that the good toughness of carbide-free bainite steels can increase the wear resistance under rolling/sliding, because the high hardness and good combination of the white-etching layers are formed at the surface. The studies further suggest that the retained austenite (RA) has been identified as an important factor in the formation of white etching layer. Leiro et al. [10, 11] reported that the wear resistance can be improved by transformation of austenite into martensite during wear, and the hardness of the white etching layer could be increased by the decrease of RA fraction, so the wear resistance of the steels were enhanced. Solano-Alvarez et al. [12] studied that the white-etching layers on the bearing steel spalling from the surface as the cracks bring together into larger networks, and the less RA exist in the steels is the main reason.

In general, the microstructure and the fraction of RA influenced the formation of the white-etching layers, and then has impact on the wear

resistance. Meanwhile, it is worth noting that the combined thermal and mechanical stability of the RA, and the mechanically induced austenite transformation is significantly effected by the temperature [13]. The wear resistance on the surface of bainitic steel in high wear test temperatures need to be resolved.

In our previous study, the laser surface treatments with advantage of self-quenching, intense energy flux and small heat affected zone have been used to surface modification of a medium-carbon bainite steel [14]. The austenite nano-twin has been detected abound in the surface modified bainite, and the hardness of this layer is reached 600 HV. However, the wear resistance of bainitic steel, which is improved by laser surface hardening was still less reported.

In this paper, a medium-carbon bainite and the Laser surface melting combined with isothermal treatment (LSMCIT) bainite were used to characterize the wear resistance of the samples at different temperature, and then the RA transformation induced by wear deformation at different temperature are studied.

2. Experimental procedure

2. 1 Experimental materials

The steel were prepared as a cast ingot, the samples were homogenized at 1200 ºC for 24 h. The actual chemical composition of the

steel used in this work is given in Table 1.

The M_s temperature of the mid-carbon high-silicon steel was measured by Gleeble-3800 thermal mechanical simulator equipped, which is 230ºC. The steel was austenitized at 1000ºC for 15min and then isothermally transformed at 250ºC for 24h to obtain a bainite microstructure, marked as Sample A. The steel samples with the dimension of 40 × 20 × 10 mm^3 were machined and cleaned in ethyl alcohol, and then the samples were laser remelted by CO_2 laser device in an Ar protection box. The laser process parameters are listed in Table 2.

The steel was laser remelted in an Argon protection box and followed isothermal transformation at 250ºC for 24h, and the sample was air cooled to room temperature after the isothermal treatment, marked as Sample B.

2. 2 Experimental methods

Filed emission scanning electron microscopy (FESEM, Hitachi S4800) and transmission electron microscopy (TEM, JEM-2010) were used to observe the microstructures of the samples. X-ray diffractometer (XRD, D/max-2500/PC) with Cu Kα radiation at 40 kV and 20 mA was performed to determine the phase constitution. During the test, $40°<2\theta<120°$ with a step size of 0.02° was set and the collection time was 2s. The XRD results were analyzed by Rietveld method of refinement

combining with the Materials Analysis Using Diffraction (Maud) software from three or more XRD scan data for each sample. The weighted profile factor R_{wp} is considered to be the most relevant to follow the progress of structure refinement, which can be expressed as follow.

$$R_{wp} = \left[\frac{\sum w_i \left(x_i - y_i \right)^2}{\sum} \right]^{1/2} \quad (1)$$

where x_i is the discrete observed intensity and y_i the corresponding calculated intensity w_i is the observation weight, assigned the value x_i^{-1}.

The analysis were performed to impose a body-centred tetragonal lattice ($I\frac{4}{m}mm$) for ferrite phase during Rietveld method of refinement, as the body-centered cubic ($Im\bar{3}m$) performed to impose a higher R_{wp}. The retained austenite well-fitted using a face-centred cubic (fcc) structure.

The austenite carbon content can be calculated by Eq. 2 [3]

$$\begin{aligned} a_\gamma = {} & 3.5780 + 0.033 w_C + 0.00095 w_{Mn} - 0.0002 w_{Ni} \\ & + 0.0006 w_{Cr} + 0.0056 w_{Al} + 0.0031 w_{Mo} + 0.0018 w_V \end{aligned} \quad (2)$$

where a_γ is the lattice parameter of austenite, and W_i is the concentration of elementi in wt. %.

The austenite carbon content can be calculated by Eq. 3 [15]

$$c/a = 1 + 0.045 x_w \quad (3)$$

where *a* and *c are the* evolution of the tetragonal ferrite unit cell parameters and x_w is the concentration of carbon in wt. %.

The M_d temperature is the major critical factor to present the

deformation-induced martensite transformation, which can be calculated by Eq. 4 [16]

$$M_d = 551 - 462(C(\gamma) + N(\gamma) - 9.2Si(\gamma) - 8.1Mn(\gamma) - 13.7Cr(\gamma) - 29Ni(\gamma) - 29Cu(\gamma) - 18.5Mo(\gamma)) \quad (4)$$

Microhardness tester (FM-ARS 9000) with a load of 100 gf (0.98 N) was conducted for hardness determination, and the dwell time is 10s. 10 random positions were used to detect the microhardness of the material, and the distance between the two adjacent indentations was more than three times the length of the indentation diagonal. Nano-mechanical tester (CPX-NHT^2) equipped with a diamond Berkovich tip was conducted for hardness determination using the load of 10 mN and dwell time of 10 s during the test. A 30° angular between the linear locus of the cross-sectional nanohardness gradient and the sample surface. Therefore, the step size of the nanoindentation along the depth is only 5μm when the distance between two indentations is 10μm.

Sliding wear tests of the samples were carried out using a reciprocating friction tribometer (Anton paar tribometer) under unlubricated dry conditions to ascertain changes in the tribological behavior. The size of sliding wear test sample was 12 × 6 × 3 mm^3. The experimental parameters are listed in Table 3. A 6-mm diameter tungsten carbide ball was used for sliding against the sample. High temperature sliding wear were tested under a heating thermostat system, which is

equipped on the reciprocating friction tribometer. The characterization of dry sliding wear behavior of two samples at different temperatures, which include 20ºC, 100ºC and 200ºC, were carried out by a reciprocating friction tribometer. Fig. 1 shows the schematic diagram of worn surface morphology, which is abrased by a reciprocating friction tribometer. As the tungsten carbide ball pass through the sample surface, the metal has been seriously squeezed and the heavy plastic deformation are produced, then the wear debris can be produced and oxidized. As the tungsten carbide ball passing the surface again, the oxide particles was pushed to the forward and aside. The microstructure significantly affect on the groove characteristics of the abraded surfaces. When the friction pairs pass through the surface of the sample, the steel was removed and leaving the wear track. Therefore, the degree of wear can be clearly characterized by the scar outline of the wear track. The wear volume loss is the major critical factor to present the wear resistance of metal material, which can be calculated by Eq. 5:

$$V = (A_g - A_1 - A_2) \times L \tag{5}$$

where A_g is the cross-sectional area of the groove; A_1 and A_2 are the cross-sectional area of ridges; L is the distance of the groove.

These comments are shown in Fig. 1. A_1, A_2 and A_g were measured after the fitting of profiles scan data.

During the laser melting process, three samples were prepared and

three or more samples were tested for each wear conditions. Three or more samples were tested by microhardness, wear volume loss and nanoindentation testing.

The outlines of the wear surface were carried out using a Surface Profiler (MarSurf XC 20). Proto iXRD X-Ray stress analyzer was used to detect the RA after the wear test.

3. Results and discussions

3.1 Microstructure, phase analysis and hardness prior to sliding wear test

3. 1. 1 SEM

Fig. 2 shows the microstructures of two samples. It is observed that the microstructures of the samples consist of bainite ferrite (BF) and RA with film and blocky morphology. In Fig. 2(a), it is found that the RA is uniformly distributed in the BF, and the RA with blocky morphology can be seen obviously in Sample A. Fig. 2(b) shows a refined microstructure in Sample B, which is treated by LSMCIT, and the RA films are finer than those in the Sample A. The enlarged SEM morphology of the Sample B (insert in the Fig. 2(b)) illustrates that the nano-twins are generated greatly by LSMCIT. In contrast, the nano-twins are difficult to be observed in Sample A.

3. 1. 2 Cross-sectional micromorphology

Fig. 3 shows the typical cross-sectional micromorphology of the

Sample B. The micromorphology of the layer consists of equiax crystal, dendritic crystal and heat affected zone (HAZ), respectively. The segregation of alloying elements, such as Mn, Si and Cr on the interdendritic lead to the increase of the austenite stability, and then the bainite transformation is suppressed. The wide and penetration depth of melting zone are 2.9 0.2 mm and 245 ± 15 μm. It can be seen that the microstructure of the HAZ is bainite, and dendritic segregation end to the HAZ.

3. 1. 3 XRD analysis

Fig. 4 illustrates the XRD patterns of the samples. The phase structure is primarily composed of α-Fe and γ-Fe. Simultaneously, the phase fraction, crystallite size and lattice constant of the samples are refined by Rietveld method of refinement, as summarized in Table 4.

A more detailed observation of the α-110 and γ-200 diffraction peak of two samples are given as the inset in Fig. 4. The variation of the lattice constants could be only caused by the interstitial carbon element solution. The carbon content in the austenite and BF occupy octahedral interstices. However, the solid solubility amount of the carbon is difference in each phase. It is confirmed that more carbon is dissolved in BF as the volume fraction of RA decreasing in the layer. In Sample B, many carbon atoms are dissolved in RA and BF as the volume fraction of RA is decreased in the modified layer, and the stability of the RA is improved by the carbon

supersaturation. As the increasing of lattice distortion, Sample B has been a marked reduce in the Crystallite size of BF. The carbon atoms can be trapped by crystal defects, such as dislocations, and the BF with excellent hardness was prepared by LSMCIT.

3. 1. 4 TEM analysis

Fig. 5 shows the TEM micrographs of the samples, which are the carbide-free bainite microstructure. Fig. 5(a) shows the TEM bright field image of Sample A, which includes a mixture of RA and BF. It can be seen that the bainitic plates are long and thin, and the dislocation debris is evident in the interface of BF and the surrounding RA.

Fig. 5(b) shows the TEM bright field image of Sample B, which indicates that a large number of nano-twins appear in austenite films. The dislocations in the interface of BF and RA are increased significantly. The appearance of nano-twins represents that the typical deformation-induced microstructural features are observed. Dislocations in the interface of BF and RA can be driven by the appropriate stress to form the stacking fault at the austenite [17]. The thermal stress is generated by the laser melting which can be used as the driving force to form the stacking faults. The stacking fault successive overlapping on (111) planes referred to form nano-twins.

3. 1. 5 Hardness

The hardness of the samples can be obtained via the Microhardness tester, and the average hardness of the bainite layer is evidently increased from HV 521±15 to HV 612±19.

3. 2 Wear resistance

3. 2. 1 Three-dimensional topographies

After the wear test, the confocal laser scanning microscope was used to characterize the three-dimensional topography of all abrasion surfaces. The surface topographies are shown in Fig. 6, and the wear depth is presented as differential color profile, which can portray the unique worn surface of the samples. Fig. 6(a) and (b) illustrate the wear track topographies of two samples at 20ºC. From the Fig. 6(a), it can be seen that a broad and deep wear track is appeared in Sample A. A large amounts of the wear debris are spalled from the bottom of the wear track, which lead to increase the value of roughness on wear surface of Sample A. Compared to the Sample A, the wear track morphology of Sample B is smooth, which is shown in Fig. 6(b).

With the increasing of the temperature, the width and the surface roughness of the samples are increased. Fig. 6(c) and (d) show the wear track topographies of two samples at 100ºC. By comparison of these images, the wear track roughness of Sample B is increased lightly. The wear track topographies of two samples at 200ºC are shown in Fig. 6(e)

and (f), the wear track width of the samples are increased significantly. However, Sample B with more continuous and shallow wear track, which explains that Sample B is equipped with better wear resistance at 200ºC.

3. 2. 2 Wear volume loss

Fig. 7 shows the scar outlines of the samples at different temperatures, in which the curves are averaged from five profiles scan data for each sample. All wear scar outlines were measured to calculate the wear volume loss.

The obtained wear volume loss of the samples are presented in Table 5. It can be seen that the wear resistance of the Sample B is better than that of the Sample A. The wear volume reduction ratio of Sample B is 40.9% at 20ºC.

The wear volume loss of the samples are increased with the increasing of the temperature. As the wear volume of Sample A at 200ºC is almost tripled over that at 20ºC. By contrast, the wear volume of Sample B at 200ºC is more twice than that at 20ºC. It can be seen that the effect of temperature less on the wearability of Sample B is small. These results are consistent with the analytic result of the laser confocal.

3. 2. 3 Friction coefficient

Fig. 8 show the friction coefficient curve of two samples at different temperatures. From the Fig. 8(a), it was not significantly correlated with the friction coefficient of Sample A at different temperature, and the

friction coefficient of the samples at 20℃ is the lowest. By comparison, Fig. 8(b) shows the friction coefficient curves of Sample A at different temperatures. The increase of the test temperature has an obvious influence on the friction coefficient. The friction coefficient interpreted the real-time information of frictional resistance of the friction pair movement during the wear process. Combination with the three-dimensional topography of all abrasion surfaces, the friction coefficient is increased by the high-level roughness of the worn surface.

3. 2. 4 Abrasion morphology

Fig. 9 show the SEM micrographs of the wear track top of two samples at different temperatures, in which, the accumulation of the wear debris can be seen. Once most of the hard wear debris have been worn off, the wear mechanism has becomes to three-body abrasion, and then the abrasive wear is aggravated [12]. From the Fig. 9(a) and (b), a few wear debris are accumulated at the wear track top of Sample B. With the increasing of the temperature, the amount of debris accumulation are increased in both samples, however, a greater amount of debris accumulation is appeared at the Sample A, which are shown in Fig. 9(c)-(f).

Fig. 10 shows the wear track bottom morphologies of two samples at three temperatures. From Fig. 10(a) and (b), the wear track of the Sample A is wider than that of the Sample B. The worn surface of Sample A is

subjected to indentation damage due to the accumulation of hard wear debris, and the spalling damage become the main cause of abrasion. Compared with Sample A, some shallow grooves are generated, but no fracture chipping pits exist in Sample B. In spite of the Sample B equipped with high hardness, the brittle fracture has never been detected.

Fig. 10(a), (c) and (e) show the wear track bottom morphologies of Sample A at three temperature, in which, the roughness of the wear track is firstly decreased and then increased with the increasing of temperature. There are some separate peeling pits on the worn surface of Sample A at 20ºC. When the temperature reaches at 100ºC, the number of the peeling pits are increased, but the size and the depth of the peeling pits are decreased. The peeling pits become continuous and the flaking area is significantly increased at 200ºC.

In contrast, Fig. 10(b), (d) and (f) show the wear track roughness of Sample B, the number of peeling pits increases monotonically with increasing of temperature. Sample B has a relatively low surface roughness at three temperature.

Fig. 11 show the SEM micrographs of the wear tracks edge of two samples at different temperatures. From Fig. 11(a) and (b), the grooves on the wear track surface of Sample A are deeper than those of Sample B.

Fig. 11(a), (c) and (e) show the wear tracks edge morphologies of Sample A at three temperatures. It can be seen that the debris are

accumulated at 100ºC, and a large number pits exhibit at the wear track edge of Sample A. When the temperature reaches at 200ºC, the debris are worn off from the edge.

From Fig. 11(b), (d) and (f), the roughness of wear track edge of Sample B shows a gradual worsening trend with the increasing of temperature. The debris accumulation at wear track edge are not continuous at 20ºC. With the increase of the temperature, the wear edge becomes smooth and continuous at 100ºC. As the temperature further increase, the pits are appeared on the wear track edge at 200ºC.

3. 3 Sub-surface characterization

3. 3. 1 Cross profile SEM micrograph

Fig. 12 show the cross profile SEM micrographs of two samples at three temperatures. The worn surface profiles of cross section microstructure of two samples at 20ºC are presented in Fig. 12(a) and (b). It reveals that the layers are quite adherent to the underlying material. The deformed layer beneath the surfaces is limited with $\leqq 5\mu m$ in Sample A, and the white-etching layer is attached to Sample B surface. The morphology of the deformation layer in Sample A is shown a wavy shape. It proves that the wear debris has been worn off from the surface, the friction pair is direct contact with the surface of the sample. From Fig. 12(b), the white-etching deformation layer is the reason that the wear

resistance of Sample B can be improved significantly. The white-etching layer is adherent to matrix materials and the surface layers are difficult to remove by the reciprocating friction, which may account for the relatively higher hardness. The harder surface can firmly retain the protective transfer layer, thereby reducing direct contact between the sample and the ball. Compared with Sample A, the wear resistance of Sample B is increased, which agrees with the features of worn surfaces.

In Fig. 12(c), the worn surface profiles of cross section microstructure of Sample A at 100ºC are formed white-etching layer, and a small deformation area is existed below the white-etching layer. However, the white-etching layer disappears at 200ºC, which is shown in Fig. 12(e). Meanwhile, the deformation layer beneath the surfaces is obviously wider.

From the Fig. 12(b) and (d), the thickness of the white-etching layer of Sample B is increased with the increasing of the temperature. The plastic deformation layer is adherent to matrix materials and the surface layers are difficult to remove by the reciprocating friction, which may account for the relatively higher hardness. The carbon is supersaturated in BF which significantly increases the average hardness of the Sample B. Meanwhile, the smaller amount of metastable phase, mainly included RA, exist in, which improves the resistance of abrasion deformation. As the temperature is 200℃, an obviously visible deformation area is existed

below the white-etching layer. The support strength of the sample is reduced as the increase in temperature, resulting in plastic deformation of the sub-surface.

3. 3. 2 Sub-surface nanohardness

Fig. 13 shows the matrix and the sub-surface nanohardness of two samples after the wear test at three temperatures. In Sample A, the hardness of the sub-surface is significantly higher than that of the matrix. The hardness of the sub-surface is reached up to 7.96 0.85 GPa and the hardness of the matrix only for 6.68 0.31GPa. The error value represents higher fluctuation of sub-surface hardness. Compared to the Sample A, the difference value of the hardness between the sub-surface and the matrix of Sample B is reduced, the hardness of the sub-surface is 8.21 0.35 GPa and the hardness of the matrix is 7.57 0.33GPa. The sub-surface hardness after the wear test of Sample A is first increases and then decreases when the temperature increases. However, the sub-surface hardness after the wear test of Sample B change little at different temperatures.

The white-etching layer on the wear surface to be able to improve the wear resistance. However, the surface plastic deformation can be induced by the normal stress of the friction pair. A wide surface deformation layer can be induced by the normal stress of the friction pair

as the relatively lower hardness of Sample A. Therefore, the white-etching layer was peeling off from the surface of the sample. The harder surface of the Sample B can provides higher mechanical support, and the deformation is small.

3. 4 Analyzed of RA

The phase transformations of the worn surfaces have been analysed by Proto iXRD X-Ray stress analyzer. Fig. 14 shows the volume fraction of RA in the worn surface of two samples. It can be seen that the volume fraction of RA is decreased apparently during the reciprocating friction and wear experiment. For the Sample A, the volume fraction of RA is decreased from 19.83 ± 2.15vol. % to 6.31 ± 3.86 vol. % at 20ºC. In contrast that of RA in Sample B is reduced from 12.68±0.62 vol. % to 6.91±3.15 vol. %, and less than half of RA is transformed in Sample B at 20ºC.

When the wear temperature is 100ºC, the volume fraction of RA after the wear test is decreased to 5.03±4.15 vol. %. However, that of RA at 200ºC is 10.06±6.26 vol. %. Compared to Sample A, the volume of RA in the Sample B is a slight increased with the increasing of temperature.

The stability of RA can be improved by carbon solid solution, and the transformation of the RA is difficult to occur.

The carbon atom in the austenite occupies octahedral interstices [18]. Caballero et al. [2] reported that there is no significant segregation of

either substitutional elements, such as Si, Mn and Cr to the austenite–ferrite interface. A more in-depth study has found that no partitioning of alloying elements solute are observed between cementite and ferrite after tempering at 400 ºC for 1 h [18]. Therefore, the stability of austenite is increased at low temperatures.

The M_d temperature is the major critical factor to present the deformation-induced martensite transformation.

The carbon content and the M_d temperature of the RA in two samples are calculated and listed in Table 6.

In Sample A, the M_d temperature of RA is 123^{o}C, and RA has a low resistant to deformation induced martensite transformation at 20ºC and 100ºC. By careful observations of the Fig. 14, the volume of RA in the worn surface of Sample A is decreased when the temperature is 100ºC. The formation of martensite lead to the increasing of the wear resistance. Austenite stability is relatively higher at 200ºC than at those 20 ºC and 100ºC, as the wear temperature higher than the M_d temperature of the RA. It is difficult to occur the deformation induced martensite at 200ºC. Combining with the sub-surface nanohardness and SEM micrographs of the wear track, the surface of the sample is extruded by the friction pairs due to an absence protective of the martensite layers in Sample A at 200ºC. It is worth noting that the amount of austenite retained at 100ºC in Sample B is less than that in Sample A. Combining with the sub-surface

characterization and wear volume, it can be deduced that the deformation induced martensite occurrs in Sample A at 100ºC between the white-etching layer and the matrix, and then the wear volume reduction ratio (%) in samples B at 100ºC is only 26.3% relative to the Sample A at the same temperature.

In contrast, the harder surface of the Sample B can provides higher mechanical support. From the Table 6, the deformation induced phase transformation appears on Sample B only at 20ºC. The white-etching layer is supported by the excellent hardness surface and the formation of deformation induce martensite. So the white-etching layer is not easily worn off from the substrate. The white-etching layer can be acted as the layer of anti-attrition to improve the wear resistance. The Sample B equipped with good wear resistance at the high temperature, and the increase in temperature leads to an increase in sub-surface deformation. In addition, it is generally known that the RA and the shear bands are ductile phases and the presence of these phases is relieved the embrittlement caused by the carbon supersaturation of the BF.

4. Conclusions

(1) Bainite layer with refined microstructure and high hardness is obtained by LSMCIT, and much carbon are dissolved in RA and BF as the volume fraction of RA is decreased in the modified layer

(2) The wear volume reduction ratio of LSMCIT sample is 40.9% at

20ºC, and the nanobanite layer is equipped with good wear resistance at 20ºC, 100ºC and 200ºC.

(3) The embrittlement is relieved by the ductile phases, such as RA and shear bands, and the cracking and spalling can be avoided when the tungsten carbide ball pass through the LSMCIT sample surface.

(4) The harder surface of the LSMCIT sample can provides higher mechanical support, and the formation of white-etching layer on surface are difficult to remove by the reciprocating friction, and it is the main factor to improve the wear resistance.

Acknowledgement

This work was supported by the National Natural Science Foundations (Grant Nos. 51471148 and 51375425), P. R. China, Hebei province natural science foundation of China (No. E2015203156 and E2017203129), the basic research foundation of Yanshan University (No.16LGA002).

References

[1] F.G. Caballero, H.K.D.H. Bhadeshia, Very strong bainite, Current Opinion in Solid State and Materials Science, 8 (2004) 251-257.

[2] F. Caballero, M. Miller, S. Babu, C. Garciamateo, Atomic scale observations of bainite transformation in a high carbon high silicon steel, Acta Materialia, 55 (2007) 381-390.

[3] C. Garcia-Mateo, M. Peet, F.G. Caballero, H.K.D.H. Bhadeshia, Tempering of hard mixture of bainitic ferrite and austenite, Materials Science and Technology, 20 (2004) 814-818.

[4] F.G. Caballero, H.K.D.H. Bhadeshia, K.J.A. Mawella, D.G. Jones, P. Brown, Very strong low temperature bainite, Materials Science and Technology, 18 (2002) 279-284.

[5] C. García-Mateo, F.G. Caballero, H.K.D.H. Bhadeshia, Development of Hard Bainite, Isij International, 43 (2003).

[1] F.G. Caballero, H.K.D.H. Bhadeshia, Very strong bainite, Current Opinion in Solid State and development of a low-temperature bainitic microstructure in the surface layer of low-carbon steel, Scripta Materialia, 59 (2008) 294-296.

[7] S. Hernandez, A. Leiro, M.R. Ripoll, E. Vuorinen, K.-G. Sundin, B. Prakash, High temperature three-body abrasive wear of 0.25C 1.42Si steel with carbide free bainitic (CFB) and martensitic microstructures, Wear, 360-361 (2016) 21-28.
[8] S. Das Bakshi, P.H. Shipway, H.K.D.H. Bhadeshia, Three-body abrasive wear of fine pearlite, nanostructured bainite and martensite, Wear, 308 (2013) 46-53.
[9] L.C. Chang, The rolling/sliding wear performance of high silicon carbide-free bainitic steels, Wear, 258 (2005) 730-743.
[10] A. Leiro, E. Vuorinen, K.G. Sundin, B. Prakash, T. Sourmail, V. Smanio, F.G. Caballero, C. Garcia-Mateo, R. Elvira, Wear of nano-structured carbide-free bainitic steels under dry rolling–sliding conditions, Wear, 298-299 (2013) 42-47.
[11] A. Leiro, A. Kankanala, E. Vuorinen, B. Prakash, Tribological behaviour of carbide-free bainitic steel under dry rolling/sliding conditions, Wear, 273 (2011) 2-8.
[12] W. Solano-Alvarez, E.J. Pickering, M.J. Peet, K.L. Moore, J. Jaiswal, A. Bevan, H.K.D.H. Bhadeshia, Soft novel form of white-etching matter and ductile failure of carbide-free bainitic steels under rolling contact stresses, Acta Materialia, 121 (2016) 215-226.
[13] R. Blondé, E. Jimenez-Melero, L. Zhao, J.P. Wright, E. Brück, S. van der Zwaag, N.H. van Dijk, High-energy X-ray diffraction study on the temperature-dependent mechanical stability of retained austenite in low-alloyed TRIP steels, Acta Materialia, 60 (2012) 565-577.
[14] X.L. Xing, Y.F. Zhou, S.Y. Gao, J.B. Wang, Y.L. Yang, Q.X. Yang, Nano-twin in surface modified bainite induced by laser surface modification, Materials Letters, 165 (2016) 79-82.
[15] C.N. Hulme-Smith, I. Lonardelli, A.C. Dippel, H.K.D.H. Bhadeshia, Experimental evidence for non-cubic bainitic ferrite, Scripta Materialia, 69 (2013) 409-412.
[16] C. Herrera, D. Ponge, D. Raabe, Design of a novel Mn-based 1GPa duplex stainless TRIP steel with 60% ductility by a reduction of austenite stability, Acta Materialia, 59 (2011) 4653-4664.
[17] F.G. Caballero, M.K. Miller, C. Garcia-Mateo, Carbon supersaturation of ferrite in a nanocrystalline bainitic steel, Acta Materialia, 58 (2010) 2338-2343.
[18] F.G. Caballero, M.K. Miller, C. Garcia-Mateo, C. Capdevila, S.S. Babu, Redistribution of alloying elements during tempering of a nanocrystalline steel, Acta Materialia, 56 (2008) 188-199.

Figure Captions

Fig. 1 schematic diagram of worn surface morphology.

Fig. 2 SEM morphologies of microstructure (a) Sample A, (b) Sample B.

Fig. 3 cross-sectional micromorphology of the Sample B

Fig. 4. XRD patterns of the three samples.

Fig. 5 TEM morphology of three samples (a) Sample A, (b) Sample B.

Fig. 6 Confocal laser scanning microscope three-dimensional topographies of the wear test (a) Sample A at 20^{o}C, (b) Sample B at 20^{o}C, (c) Sample A at 100^{o}C, (d) Sample B at 100^{o}C, (e) Sample A at 200^{o}C, (f) Sample B at 200^{o}C.

Fig. 7 Scar outlines of three samples at different wear temperature (a) Sample A, (b) Sample B.

Fig. 8 friction coefficient curve of (a) Sample A, (b) Sample B

Fig. 9 SEM micrographs of the one end of all wear tracks (a) Sample A at 20^{o}C, (b) Sample B at 20^{o}C, (c) Sample A at 100^{o}C, (d) Sample B at 100^{o}C, (e) Sample A at 200^{o}C, (f) Sample B at 200^{o}C.

Fig. 10 SEM micrographs of the bottom of all wear tracks (a) Sample A at 20^{o}C, (b) Sample B at 20^{o}C, (c) Sample B at 100^{o}C, (d) Sample A at 100^{o}C, (e) Sample A at 200^{o}C, (f) Sample B at 200^{o}C.

Fig. 11 SEM micrographs of the edge of all wear tracks (a) Sample A wear test at 20^{o}C, (b) Sample B wear test at 20^{o}C, (c) Sample A wear test at 100^{o}C, (d) Sample B wear test at 100^{o}C, (e) Sample A wear test at 200^{o}C, (f) Sample B wear test at 200^{o}C.

Fig. 12 SEM micrographs of the cross section of all wear tracks (a) Sample A wear test at 20^{o}C, (b) Sample B wear test at 20^{o}C, (c) Sample A wear test at 100^{o}C, (d) Sample B wear test at 100^{o}C, (e) Sample A wear test at 200^{o}C, (f) Sample B wear test at 200^{o}C.

Fig. 13 matrix and sub-surface nanohardness of two samples after the wear test at three temperatures.

Fig. 14 RA volume fraction of the worn surface

Table 1 Chemical compositions of the steel (wt.%)

Element	C	Si	Mn	Cr	Ni	Mo	Fe
wt. %	0.55	2.53	1.82	1.08	0.45	0.32	Bal.

Table 2 laser process parameter

laser power output	defocusing amount	laser scanning speed	laser spot diameter	overlap rate
1.8 kW	5.0 mm	10 mm/s	Φ3.0 mm	8 %~12 %

Table 3 Friction and wear test parameters

Load	Frequency	Max liner speed	Test distance	Times	Test temperature
5 N	1.6 Hz	40mm/s	8 mm	60 min	20ºC 100ºC 200ºC

Table 4 Results of Rietveld method of refinement

Sample number	Sample A	Sample B
Lattice constant of BF(Å)	a=2.864 ± 0.001 c=2.874 ± 0.001 Å	a=2.861 ± 0.001 c=2.878 ± 0.001 Å
Crystallite size of BF (nm)	98.1± 2.5	50.3 ± 2.5
Carbon contents of BF (wt. %)	0.077	0.132
Microstrain of BF	0.00201	0.00285
Lattice constant of RA (Å)	3.6120 ± 0.001	3.6141 ± 0.001 Å
Crystallite size of RA (nm)	77.5 ± 2.5	37.5 ± 2.5
Microstrain of RA	37.5 ± 2.5	0.00314
Volume fraction of RA (%)	19 ± 0.83%	13 ± 0.68%
R_{wp}	10.09%	10.23%

Table 5 Wear volume loss of the samples at different wear test temperature

Wear test temperature	Wear volume Sample A (mm^3)	Wear volume Sample B (mm^3)	Wear wolume reduction ratio (%)
20ºC	1.142 ± 0.081	0.675 ± 0.053	40.9%
100ºC	1.405 ± 0.098	1.036 ± 0.077	26.3%
200ºC	3.309 ± 0.141	1.746 ± 0.126	47.3%

Table 6 carbon content and the M_d temperature of the RA in the samples

Sample number	Carbon content of RA (wt. %)	M_d temperature of RA (^oC)
Sample A	0.838	123
Sample B	0.902	86

Figure 1
Click here to download high resolution image

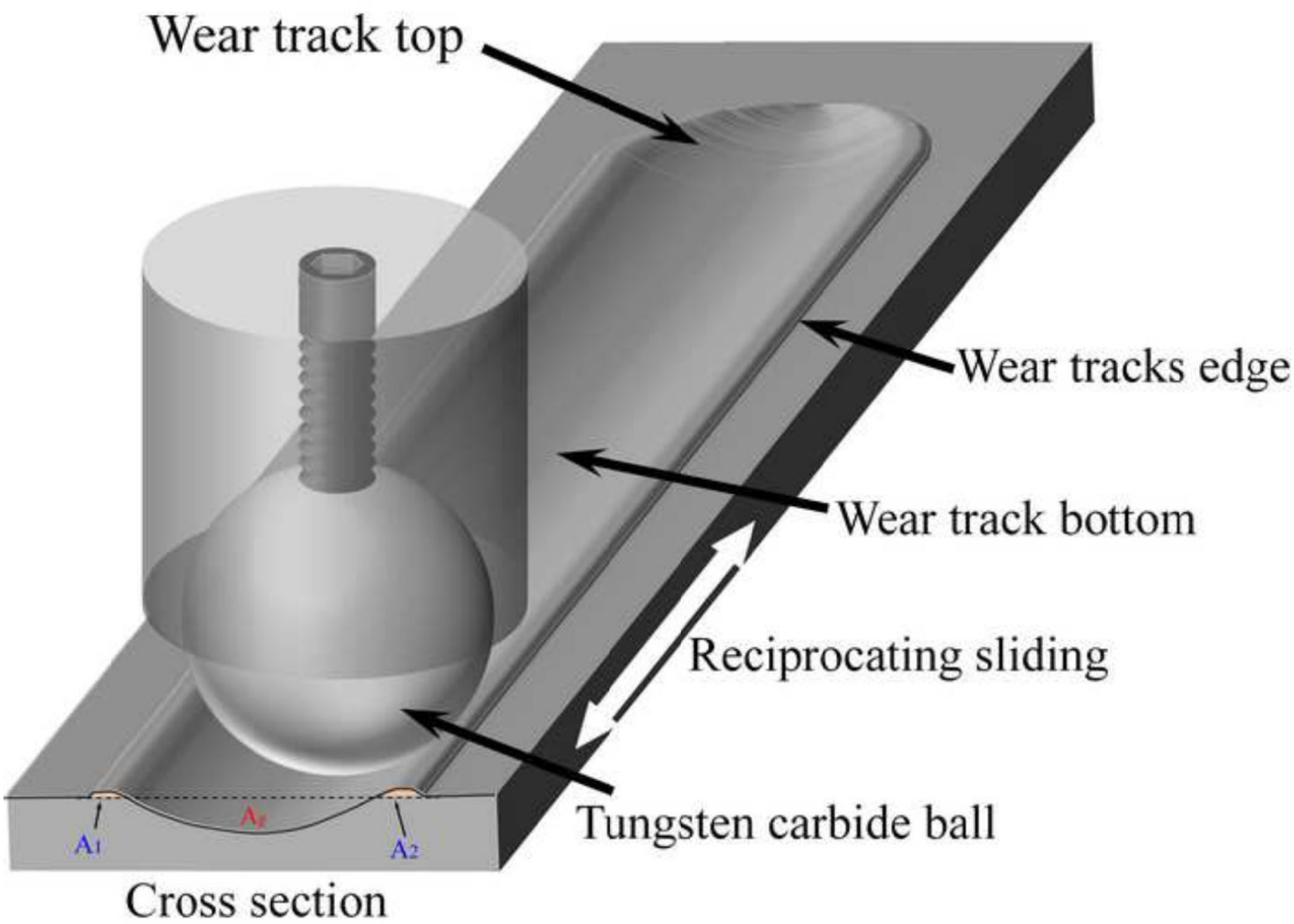

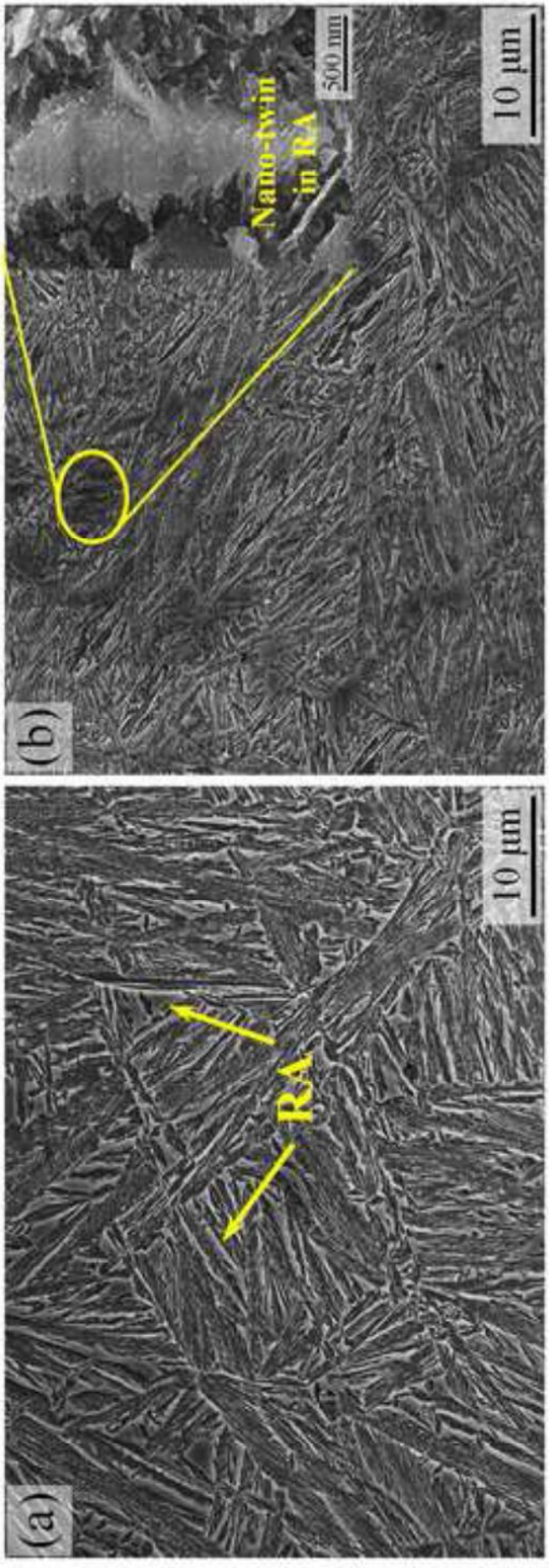

Figure 2
Click here to download high resolution image

Figure 3
Click here to download high resolution image

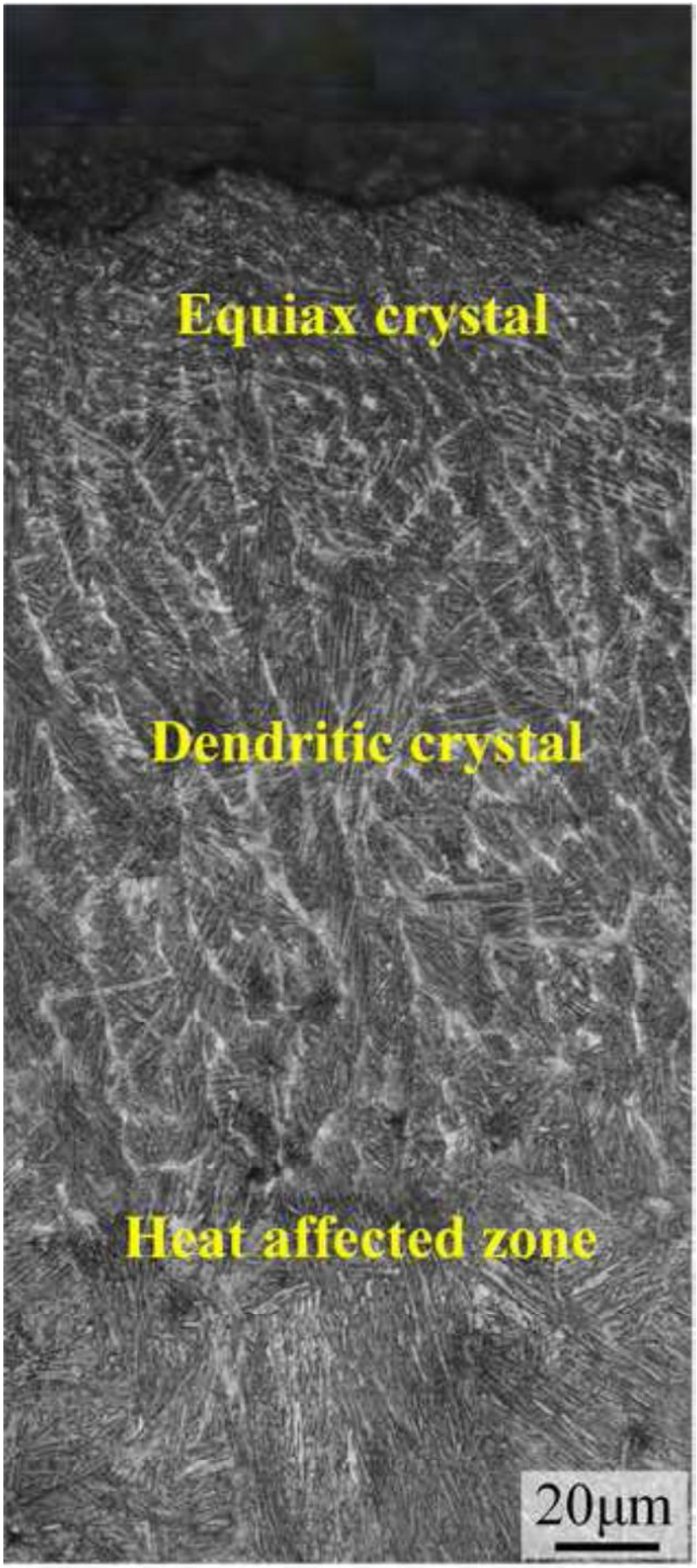

Figure 4
Click here to download high resolution image

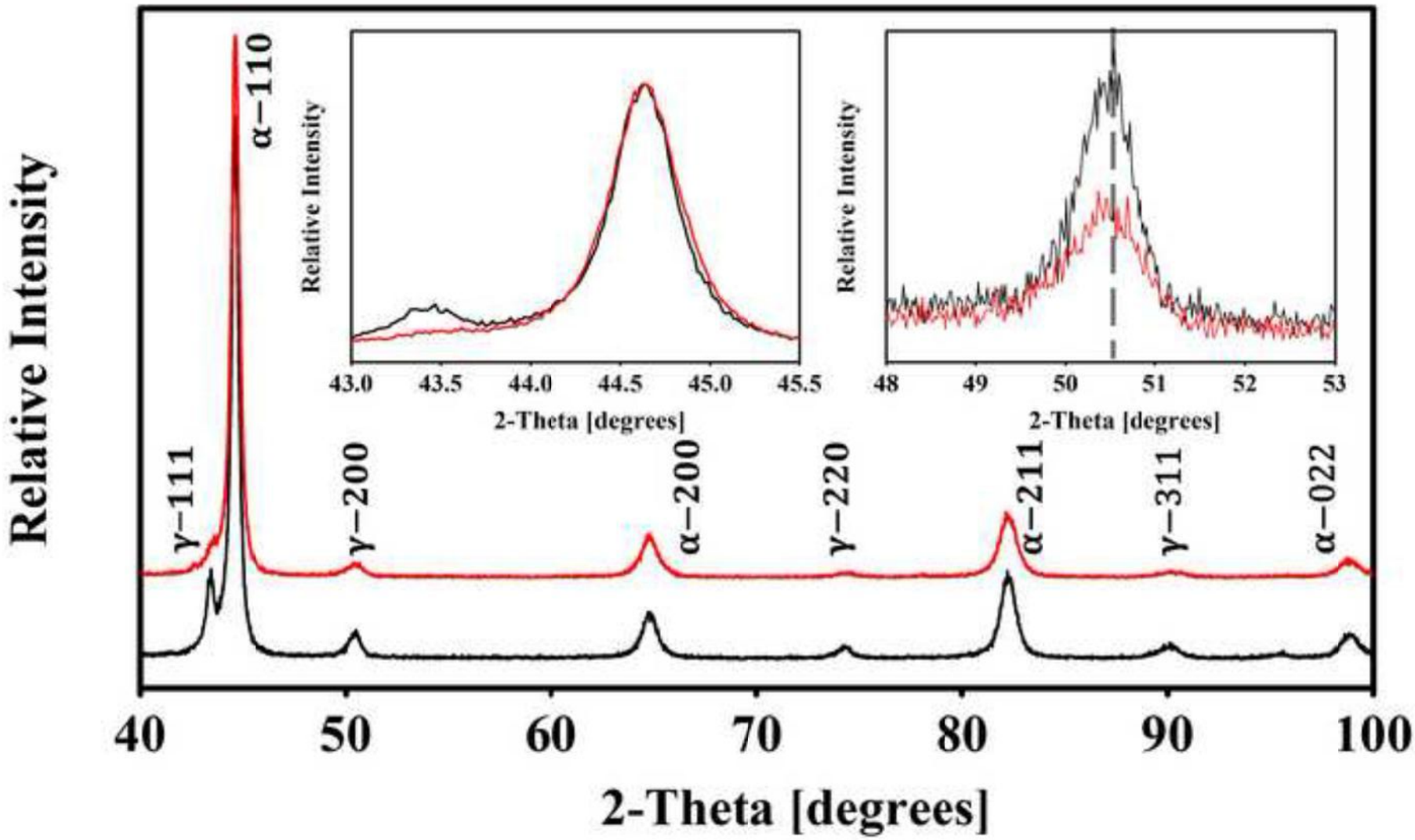

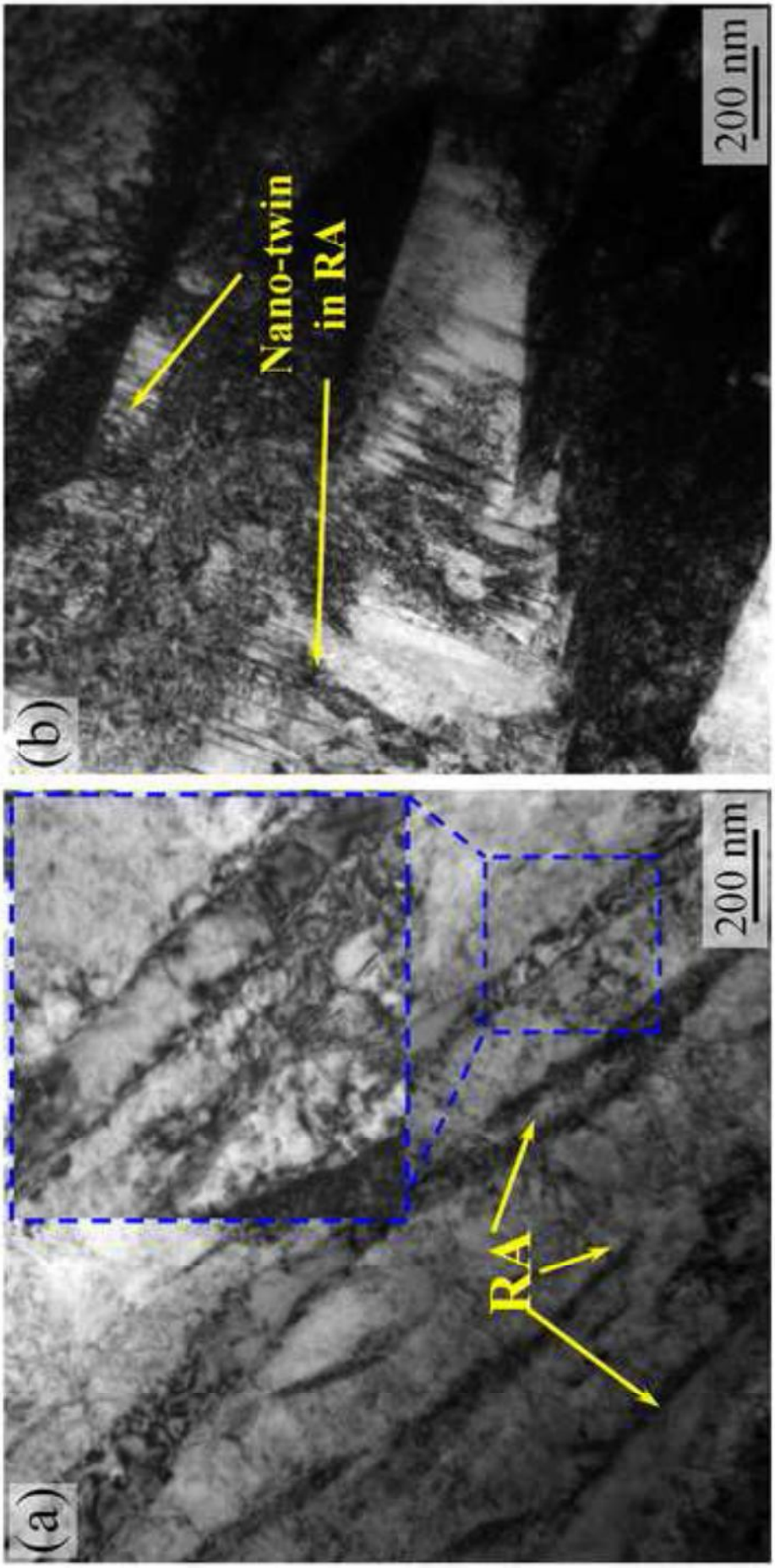

Figure 5
Click here to download high resolution image

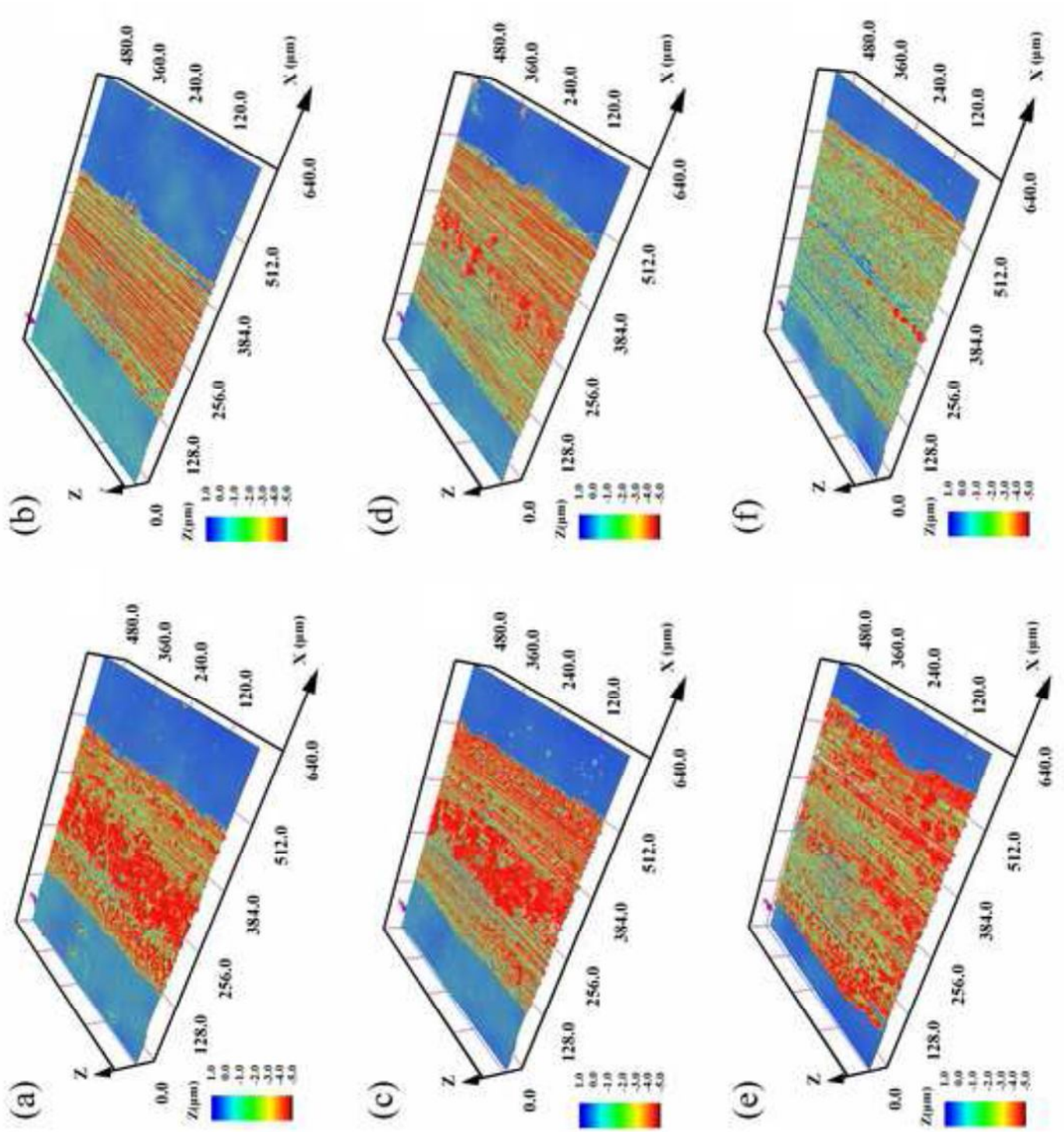

Figure 6
Click here to download high resolution image

Figure 7
Click here to download high resolution image

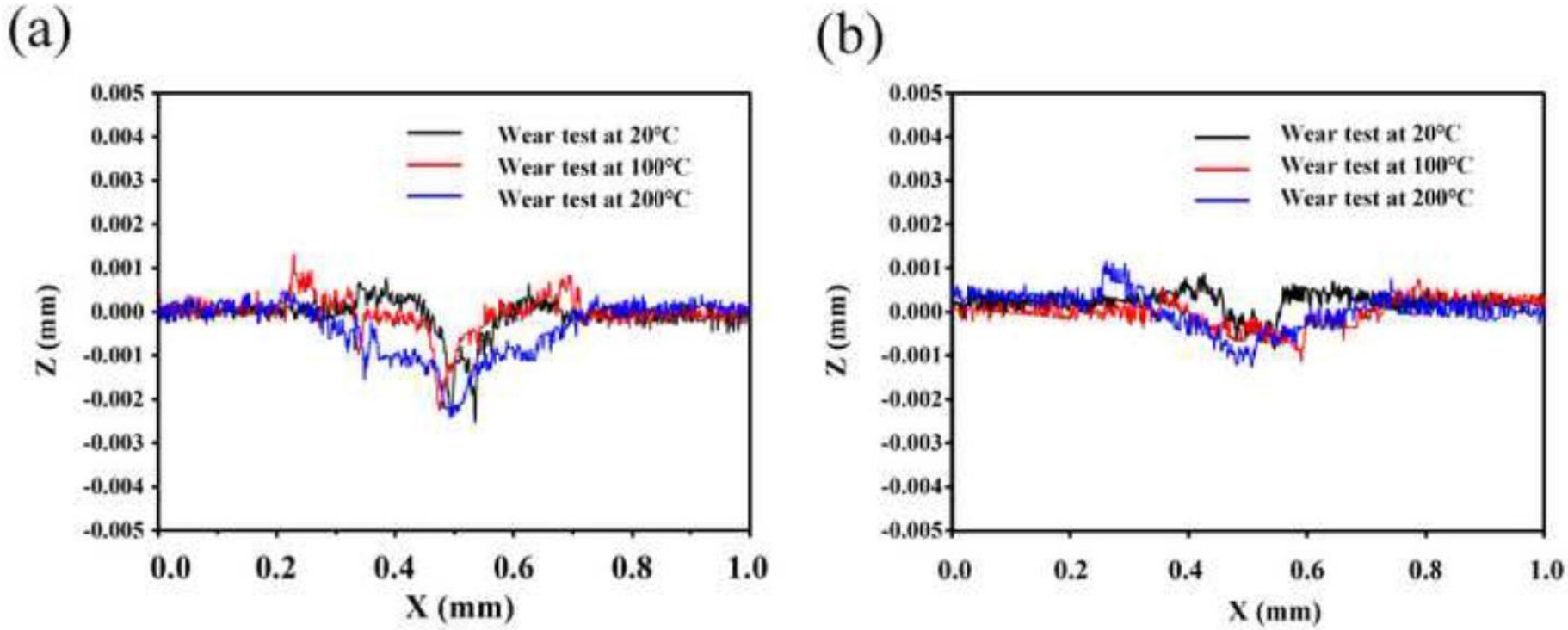

Figure 8
Click here to download high resolution image

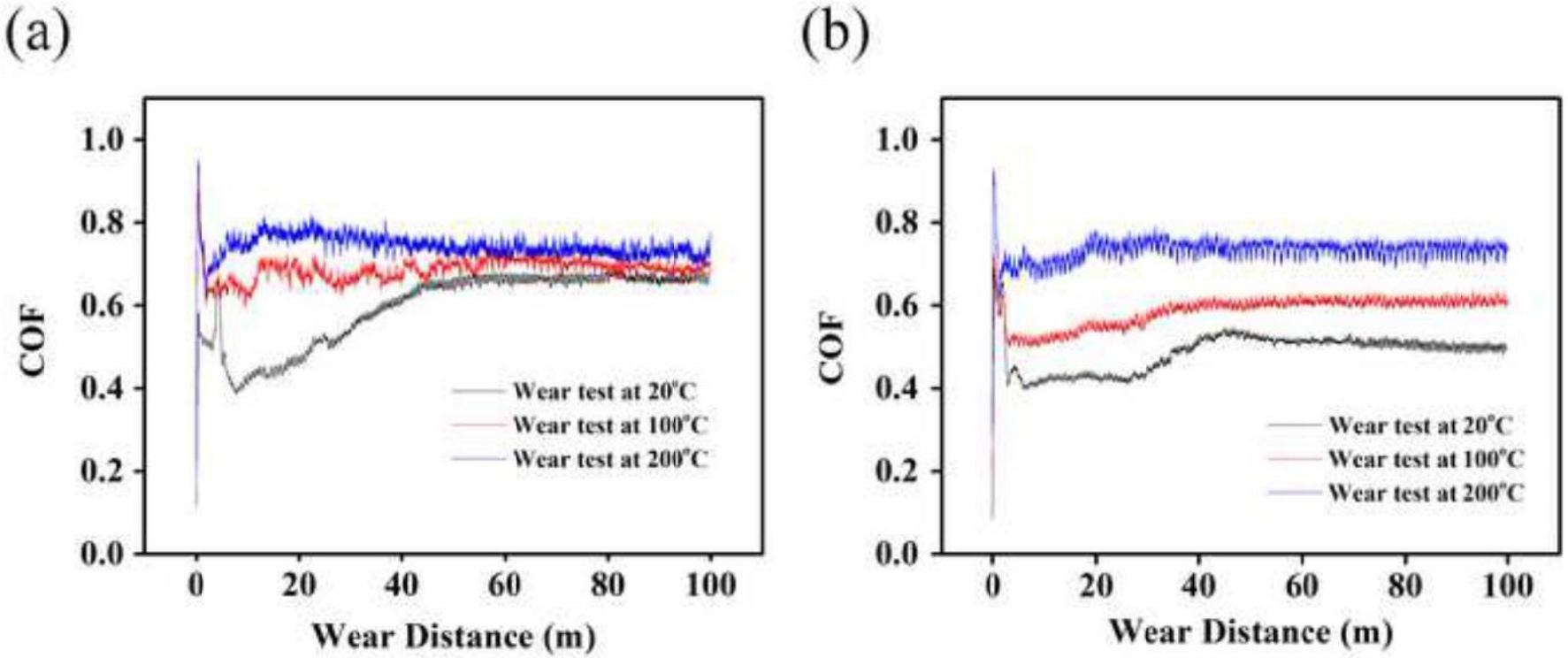

Figure 9
Click here to download high resolution image

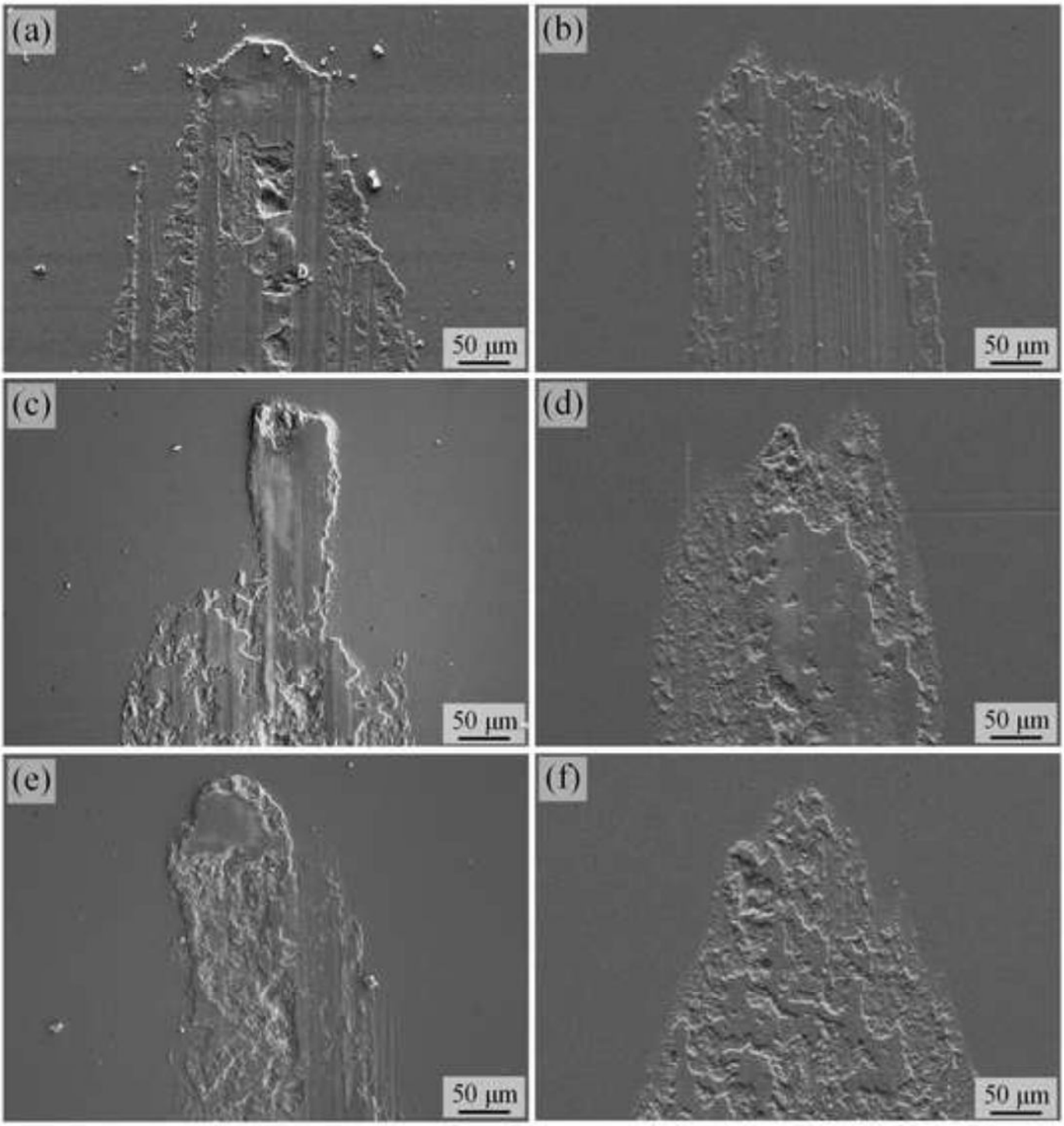

Figure 10
Click here to download high resolution image

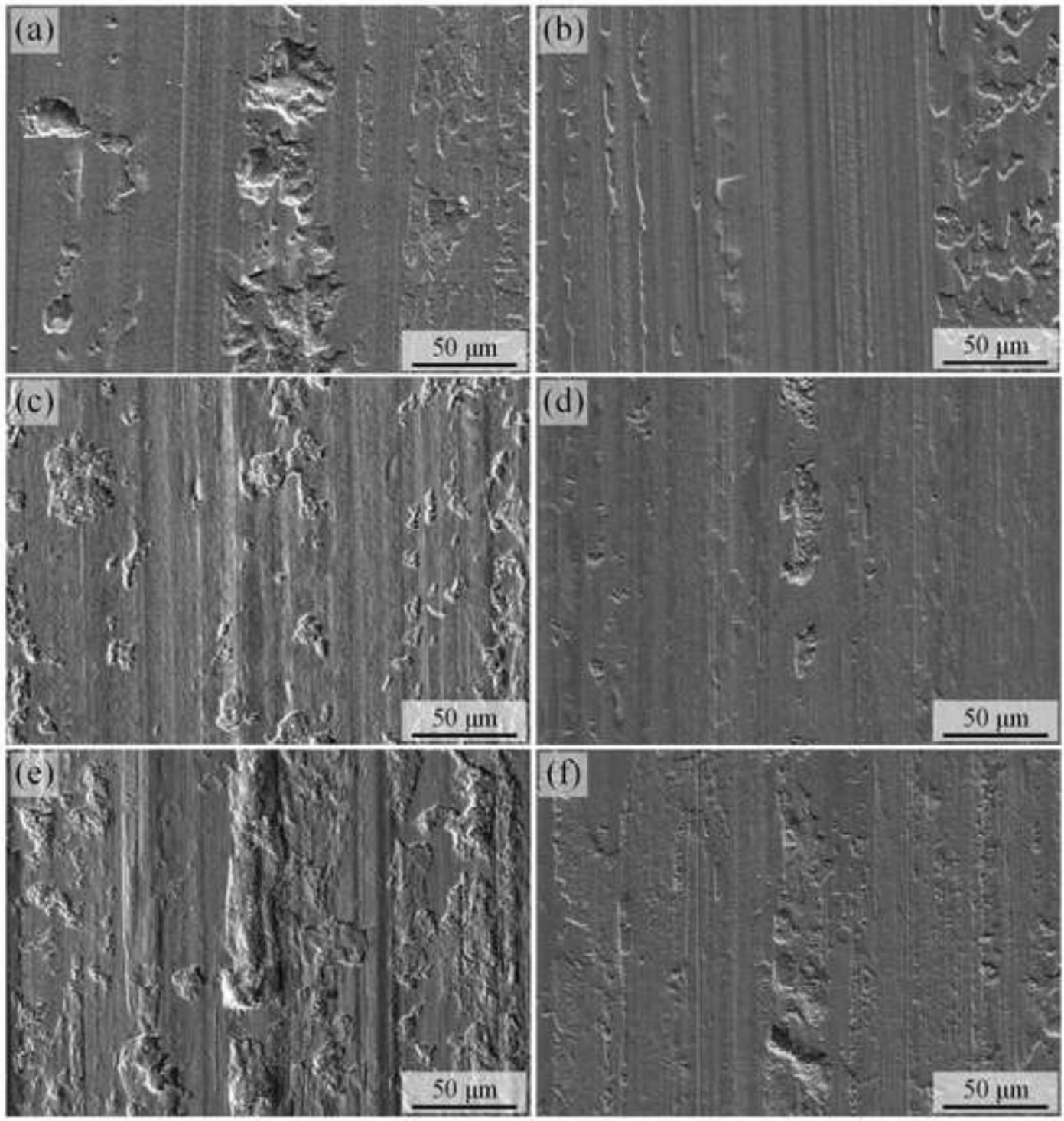

Figure 11
Click here to download high resolution image

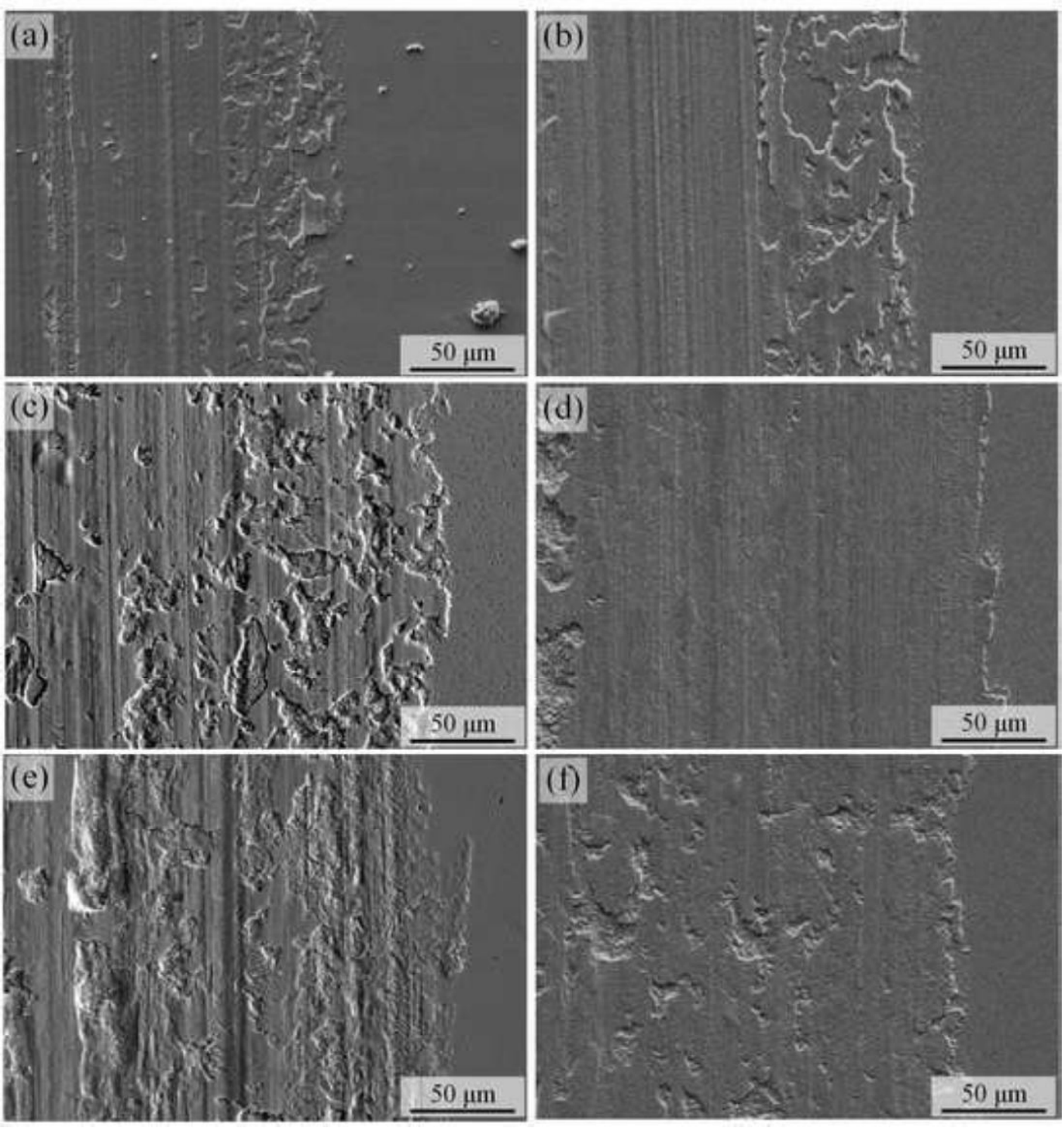

Figure 12
Click here to download high resolution image

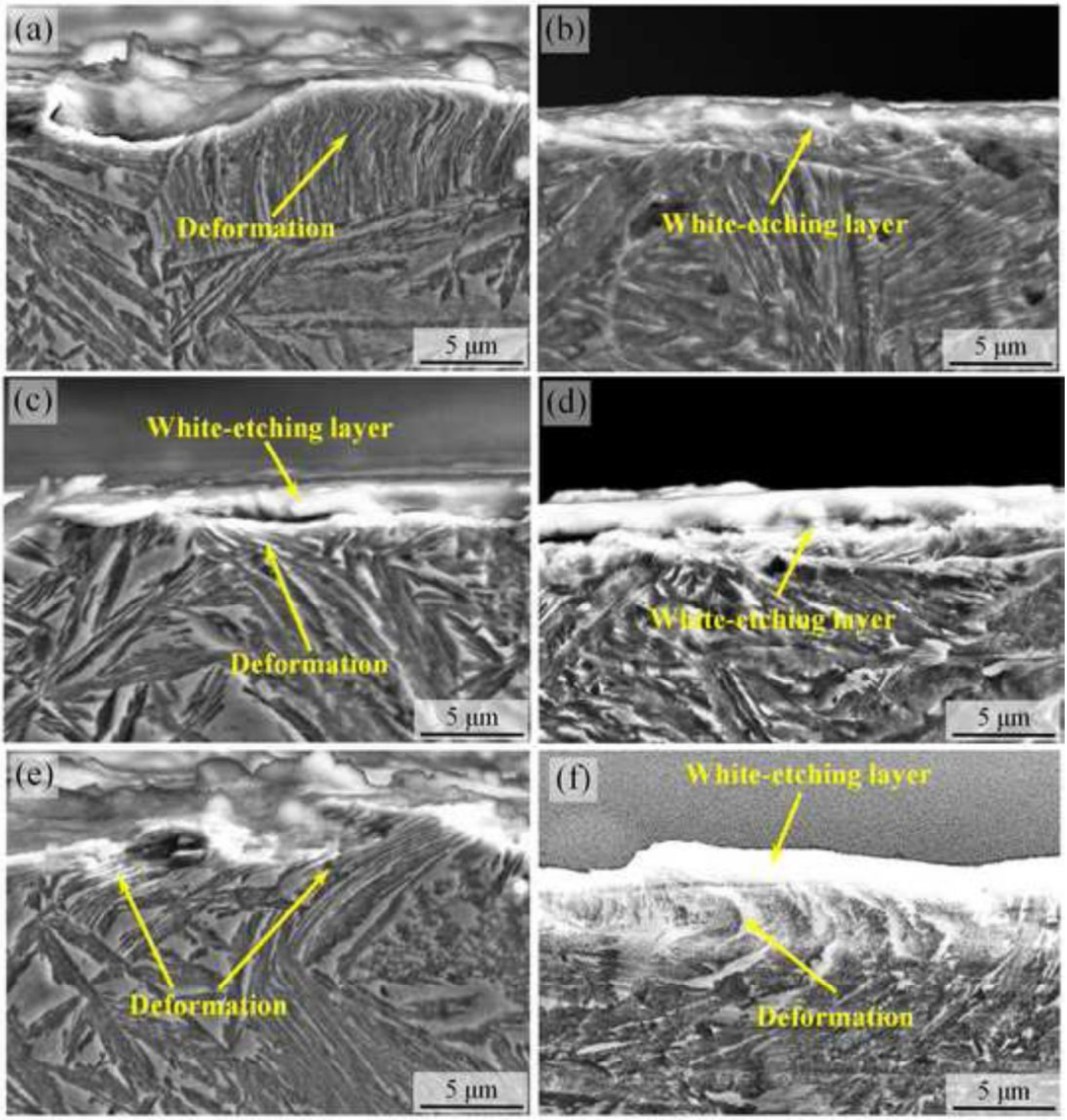

Figure 13
Click here to download high resolution image

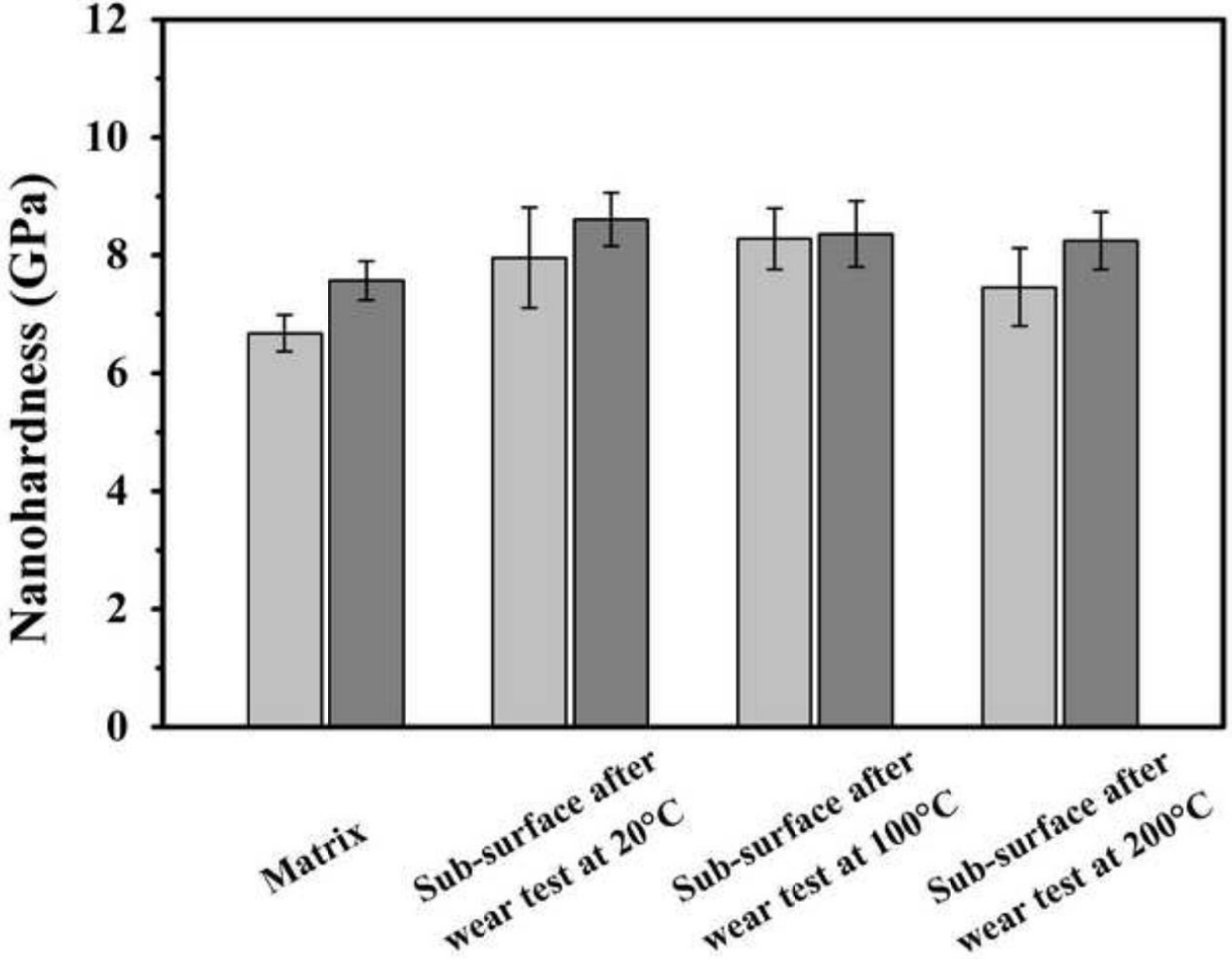

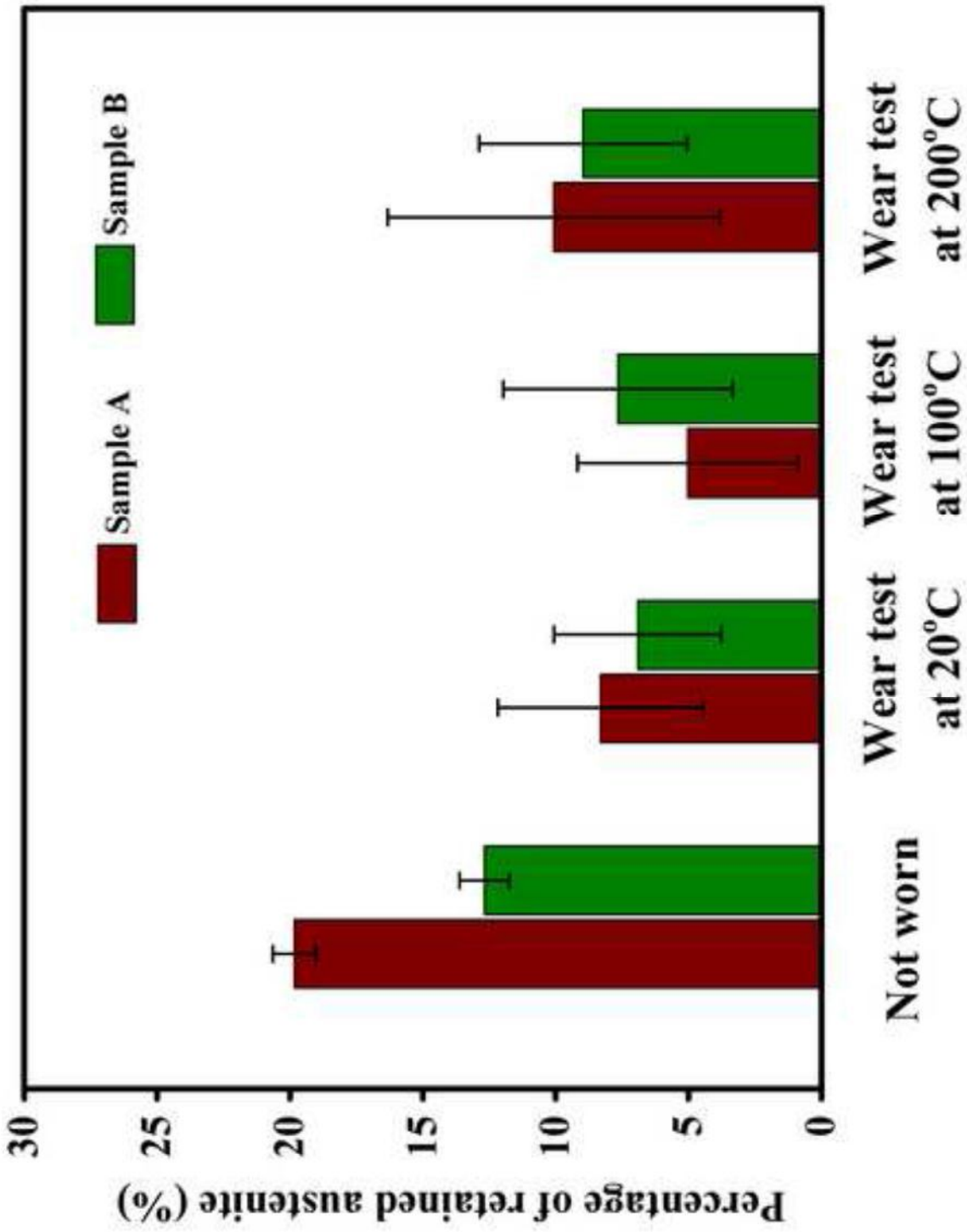

Figure 14
Click here to download high resolution image